Ramos Domke, C. M., Mechie, J., Feng, M. (2016): Shear wave velocity and Poisson's ratio models across the southern Chile convergent margin at 38°15′S. - *Geophysical Journal International*, *204*, 3, pp. 1620–1635.

DOI: http://doi.org/10.1093/gji/ggv541

Geophysical Journal International

Geophys. J. Int. (2016) **204,** 1620–1635 doi: 10.1093/gji/ggv541
GJI Seismology

Shear wave velocity and Poisson's ratio models across the southern Chile convergent margin at 38°15′S

C. Ramos,[1,2] J. Mechie[1] and M. Feng[3]

[1]*Deutsches GeoForschungsZentrum GFZ, Section Geophysical Deep Sounding, Telegrafenberg, D-14473 Potsdam, Germany. E-mail: ramos@gfz-potsdam.de*
[2]*Institute of Earth and Environmental Science, University of Potsdam, Potsdam, Germany*
[3]*Institute of Geomechanics, Chinese Academy of Geological Sciences, Beijing, China*

Accepted 2015 December 16. Received 2015 November 24; in original form 2015 July 16

SUMMARY

Using active and passive seismology data we derive a shear (S) wave velocity model and a Poisson's ratio (σ) model across the Chilean convergent margin along a profile at 38°15′S, where the M_w 9.5 Valdivia earthquake occurred in 1960. The derived S-wave velocity model was constructed using three independently obtained velocity models that were merged together. In the upper part of the profile (0–2 km depth), controlled source data from explosions were used to obtain an S-wave traveltime tomogram. For the middle part (2–20 km depth), data from a temporary seismology array were used to carry out a dispersion analysis. The resulting dispersion curves were used to obtain a 3-D S-wave velocity model. In the lower part (20–75 km depth, depending on the longitude), an already existent local earthquake tomographic image was merged with the other two sections. This final S-wave velocity model and already existent compressional (P) wave velocity models along the same transect allowed us to obtain a Poisson's ratio model. The results of this study show that the velocities and Poisson's ratios in the continental crust of this part of the Chilean convergent margin are in agreement with geological features inferred from other studies and can be explained in terms of normal rock types. There is no requirement to call on the existence of measurable amounts of present-day fluids, in terms of seismic velocities, above the plate interface in the continental crust of the Coastal Cordillera and the Central Valley in this part of the Chilean convergent margin. This is in agreement with a recent model of water being transported down and released from the subduction zone.

Key words: Controlled source seismology; Seismic tomography; Computational seismology; South America.

1 INTRODUCTION

The largest earthquakes on Earth are known to be generated in subduction zones. The regions above subduction zones constitute one of Earth's most hazardous living environments due to the dangers posed by destructive earthquakes and volcanoes. Nevertheless, due to factors such as climate, resources and accessibility, such regions are often heavily populated. Thus, it becomes necessary to have a deep understanding of the structures and processes which shape the plate boundary region of a subduction zone. This is particularly true in the seismically coupled part of the subduction zone, where nearly all earthquakes with magnitude greater than 8 occur. One such area is the active continental margin of southern Chile, where on 1960 May 22 the largest earthquake ever recorded instrumentally (M_w 9.5) occurred.

With the aim of a better understanding of the structures, processes and petrophysical properties within the seismogenic coupling zone and with the possibility of improving the earthquake hazard assessment in southern Chile, several German and Chilean institutions have carried out collaborative projects in the region over the past 15 yr. The project SPOC (Subduction Processes Off Chile; Krawczyk & the SPOC Team 2003), carried out in autumn 2001, was an amphibious seismic survey focused on the seismogenic coupling zone and the forearc in the southern central Chilean margin. It had a long-term vision, which was the quantitative understanding of mega-thrust earthquake seismicity in subduction zones and its relation to processes at depth and at the surface. At the same time, the experiments within the project, in particular an onshore seismic reflection profile served as a feasibility study for a subsequent seismology project in the area called TIPTEQ.

The TIPTEQ project (from The Incoming Plate to mega-Thrust EarthQuake processes) was an integrated study carried out between the years 2004 and 2007 that aimed for the investigation of the structure and thermal state of the oceanic plate and the subduction

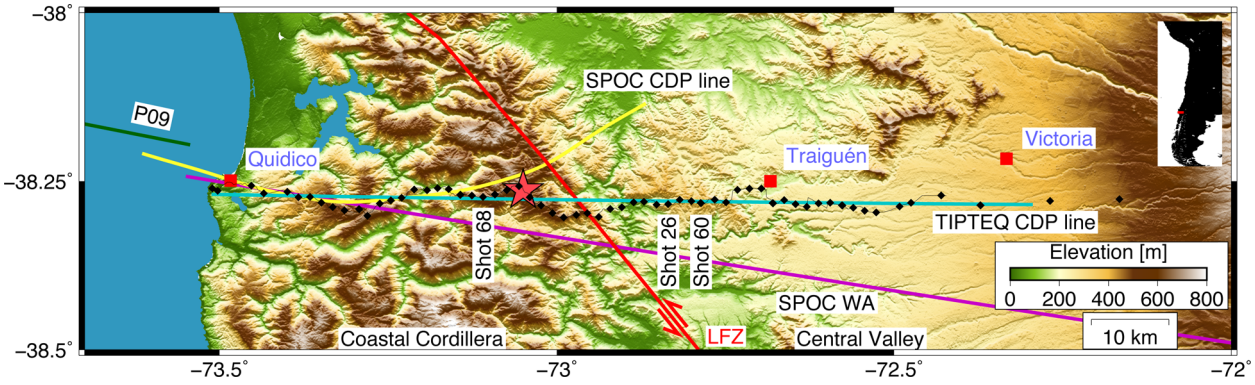

Figure 1. Location of the onshore active-source experiment of project TIPTEQ. Black line, receiver line; black diamonds, shot locations; cyan line, common depth-point (CDP) line of the TIPTEQ seismic reflection profile; red star, epicentral area of the 1960 Valdivia earthquake (Krawczyk & the SPOC Team 2003). The yellow and magenta lines mark the CDP line of the SPOC onshore seismic reflection profile and the SPOC wide-angle refraction profile (SPOC WA), respectively (Krawczyk & the SPOC Team 2003). The green line marks the easternmost part of the integrated TIPTEQ and SPOC reflection and refraction wide-angle offshore profile (Contreras-Reyes *et al.* 2008a). The red line maps the surface trace of the Lanalhue fault zone (LFZ; after Melnick & Echtler 2006). The locations of the shots mentioned in the text are labelled. Figure modified after Groß *et al.* (2008).

zone, the composition and rheology of the subducting sediment, the seismicity and nucleation of large subduction-related earthquakes, and the role of water in all of the above (Rietbrock *et al.* 2005; Scherwath *et al.* 2006). Project TIPTEQ comprised different multi-disciplinary subprojects, including active and passive source seismology onshore and offshore for structure and seismicity information, heat-flow measurements for thermal modelling, sediment probing for compositional, chemical and mechanical data, magnetotelluric soundings for subsurface resistivity and extensive multibeam bathymetric mapping throughout the entire survey area offshore (Scherwath *et al.* 2009, and references therein). For this paper, we used data from two of the seismic experiments. The first is an active source experiment carried out in January 2005 (TIPTEQ Seismic), consisting of a 95.5 km long west–east near-vertical incidence reflection (NVR) profile with explosive sources every 1.5 km at 38°15′S. This experiment aimed at imaging and identifying the structural and petrophysical properties within the Chilean seismogenic coupling zone (e.g. compressional and shear wave velocities, density, pore pressure and friction) and identifying processes occurring in the vicinity of the subduction thrust such as stress field, compaction, lithification and dehydration (Groß *et al.* 2008; see also Fig. 1). The second is a seismology experiment carried out between November 2004 and October 2005 between 37°S and 39°S (TIPTEQ Seismology), consisting of an exceptionally dense, temporary, amphibious seismic network at the south-central Chilean continental margin (Rietbrock *et al.* 2005; Haberland *et al.* 2006; see also Fig. 2).

Several research studies have been carried out using the data collected from the TIPTEQ projects. In particular, the processed onshore TIPTEQ active source data, that is, the NVR data, plus data from other shots executed at greater offsets along the NVR profile (Expanding Spread Profile, ESP), were used to obtain a high-resolution compressional-wave traveltime tomographic image along the profile (Micksch 2008). Additional to the reflection seismic data processing and the compressional-wave tomography, geological and structural interpretations were a major task in the results shown by Groß *et al.* (2008) and Micksch (2008).

In this paper, we show the results of a shear wave velocity model along the profile at 38°15′S and the procedure for obtaining this model using active and passive source TIPTEQ data. Additionally, we obtain a Poisson's ratio model along the profile using the resulting shear wave velocity model and a compressional-wave velocity model combining the results of Micksch (2008) and Haberland *et al.* (2009). The obtained models are correlated and interpreted with geological and geophysical features derived from other studies, such as onshore and offshore velocity models from wide-angle seismic data, density models from gravity data, thermal parameters and seismicity in the study area. The results will be used as important elements in future studies of petrophysical properties in the seismogenic coupling zone. In particular, it is desired to have as detailed an *S*-wave velocity model as possible for stacking and migrating the NVR *S*-wave data.

2 TECTONIC SETTING

The study area is located at 38°15′S (Fig. 1). Here the Nazca plate subducts obliquely under the South American plate with a convergence rate of 6.65 cm a^{-1} at an angle of 82.4° (Kendrick *et al.* 2003). The age of the oceanic crust that constitutes the Nazca plate at this part of the Chilean margin is ∼25 Ma (Sdrolias & Müller 2006). Perpendicular to the southern Chile margin, the western flank of the south-central Andes in the study area is subdivided from east to west in the Central Valley and the Coastal Cordillera (Fig. 1). The Central Valley is a basin formed by Oligocene-Miocene sedimentary and volcanic rocks, covered by Pliocene-Quaternary sediments (Melnick & Echtler 2006). The Coastal Cordillera is composed mainly of metamorphic rocks. Distinction is made between the western and eastern series, based on contrasting lithologies and tectono-metamorphic signatures. The western series, which is a Late-Carboniferous to Triassic basal-accretionary forearc wedge complex (Glodny *et al.* 2008), occurs southwest of 38.2°S. The main lithologies are meta-turbidites, chlorite schists and minor metabasites, with local occurrences of cherts, serpentinites and sulphide bodies (Hervé 1988; Glodny *et al.* 2008). The eastern series, composed of Permian-Carboniferous magmatic arc granitoids and associated, frontally accreted metasediments (Hervé 1988; Glodny *et al.* 2008), is located northeast of 38.2°S. The NNW–SSE striking, sinistral Lanalhue fault zone (LFZ) separates these two series. When subduction in this region initiated in the Late Carboniferous, the LFZ was a normal fault that separated the then exhuming western series from the frontally accreted eastern series. Later on, in the Early Permian, the segment of the western series-eastern series contact between 37°50′S and 39°45′S transformed into a sinistral, semi

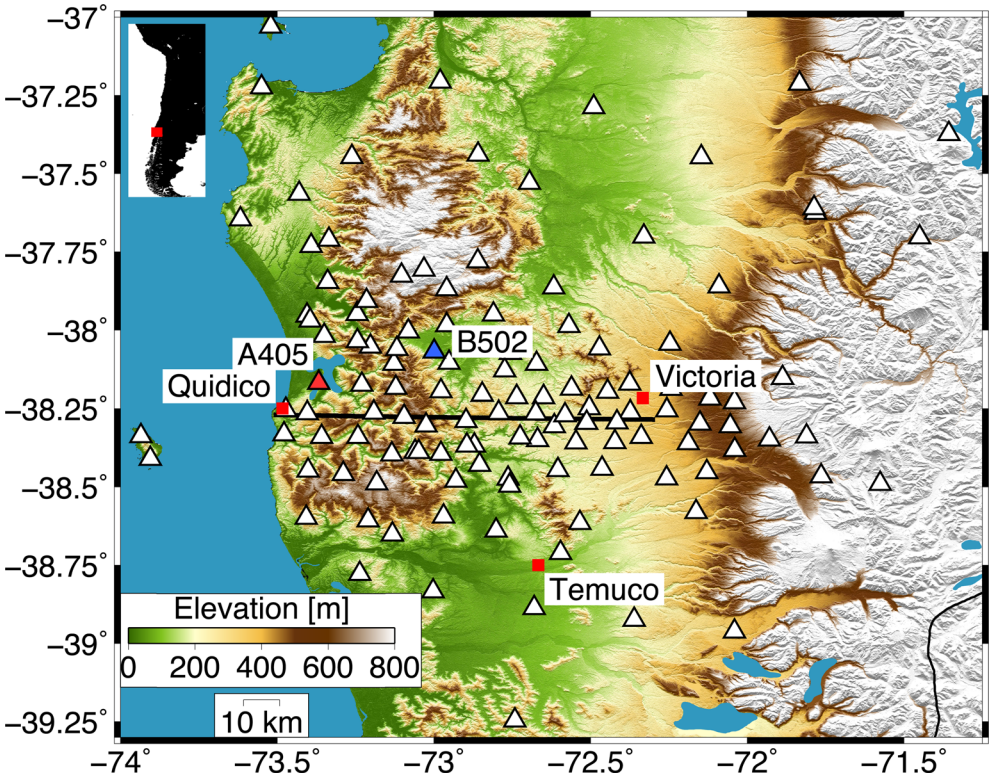

Figure 2. The 124 stations from the TIPTEQ temporary array project distributed in southern Chile between 37°S and 39°S that were used for the noise tomography. Stations referred to in the text are labelled. The black line is the CDP line of the TIPTEQ seismic reflection profile. Figure modified after Rietbrock *et al.* (2005).

ductile to brittle strike-slip fault (Glodny *et al.* 2008). Seismicity along this fault indicates ongoing activity (Haberland *et al.* 2006).

3 TIPTEQ DATA

The data used to obtain the shear wave velocity image along 38°15′S come from active and passive source experiments within the TIPTEQ project.

From the TIPTEQ Seismic experiment, 102 shots were recorded by 180 3-component channels and were used to pick shear wave traveltimes on the east–west and north–south components. These traveltime picks were then inverted using tomographic methods to obtain a detailed near-surface shear wave velocity model. The 102 shots comprised those from the NVR and ESP experiments and shots from a pilot study testing the generation of horizontally polarized shear (*SH*) waves using the Camouflet method (Dohr 1985). Fig. 1 shows the geographic location of the shots along the receiver line. See Groß *et al.* (2008) for further information about the survey setup.

From the temporary TIPTEQ seismology array, the vertical component data from February to October 2005 recorded by 124 EDL data loggers were used to carry out a dispersion analysis and then a 3-D shear wave velocity tomographic inversion. Average station spacing was around 7 km in the centre of the array and larger in the outskirts of the region of interest (40 km). The geographical location of the 124 stations is shown in Fig. 2. Further information about the TIPTEQ Seismology experiment can be found in Rietbrock *et al.* (2005), Haberland *et al.* (2006) and Haberland *et al.* (2009).

The third shear wave tomography used in our final *S*-wave velocity model was the model of Haberland *et al.* (2009). They used local earthquake data (*P*-wave and *S*-wave traveltimes picked from local events recorded by the TIPTEQ temporary array) and *P* waves generated by the controlled source explosions from the TIPTEQ Seismic experiment that were also recorded by the seismology array. From their 2-D *P*-wave velocity and v_p/v_s models we derived a shear wave velocity model along the TIPTEQ Seismic profile. This shear wave model was then combined with the shear wave models from the dispersion analysis and the traveltime tomography of the TIPTEQ controlled source data as described below to obtain a final shear wave velocity model along the TIPTEQ Seismic profile.

4 TRAVELTIME TOMOGRAPHY USING TIPTEQ CONTROLLED SOURCE DATA

From the 102 shots, a maximum of 180 arrival times per component (east–west and north–south) could have been picked per shot. This is in general not possible for various reasons such as channels that are too close to the explosive source, the presence of converted waves or interactions with the *P*-coda in the case of picking shear waves. In the case of the TIPTEQ shots, the data quality was very good and most of the time applying a Butterworth bandpass filter (2–9 Hz) to the data was enough to distinguish and pick many of the traveltimes. Some examples can be seen in Fig. 3.

A total of 12 435 shear wave arrivals was picked in the north–south component and 12 044 in the east–west component. When there was a shear wave arrival picked on both horizontal channels, the fastest of them was chosen for the tomographic inversion.

The forward part of the traveltime tomography was solved by tracing rays through the medium using a finite differences approximation of the eikonal equation (Vidale 1988; Podvin & Lecomte 1991; Schneider *et al.* 1992). Partial derivatives of the calculated traveltimes with respect to the velocity nodes were derived using

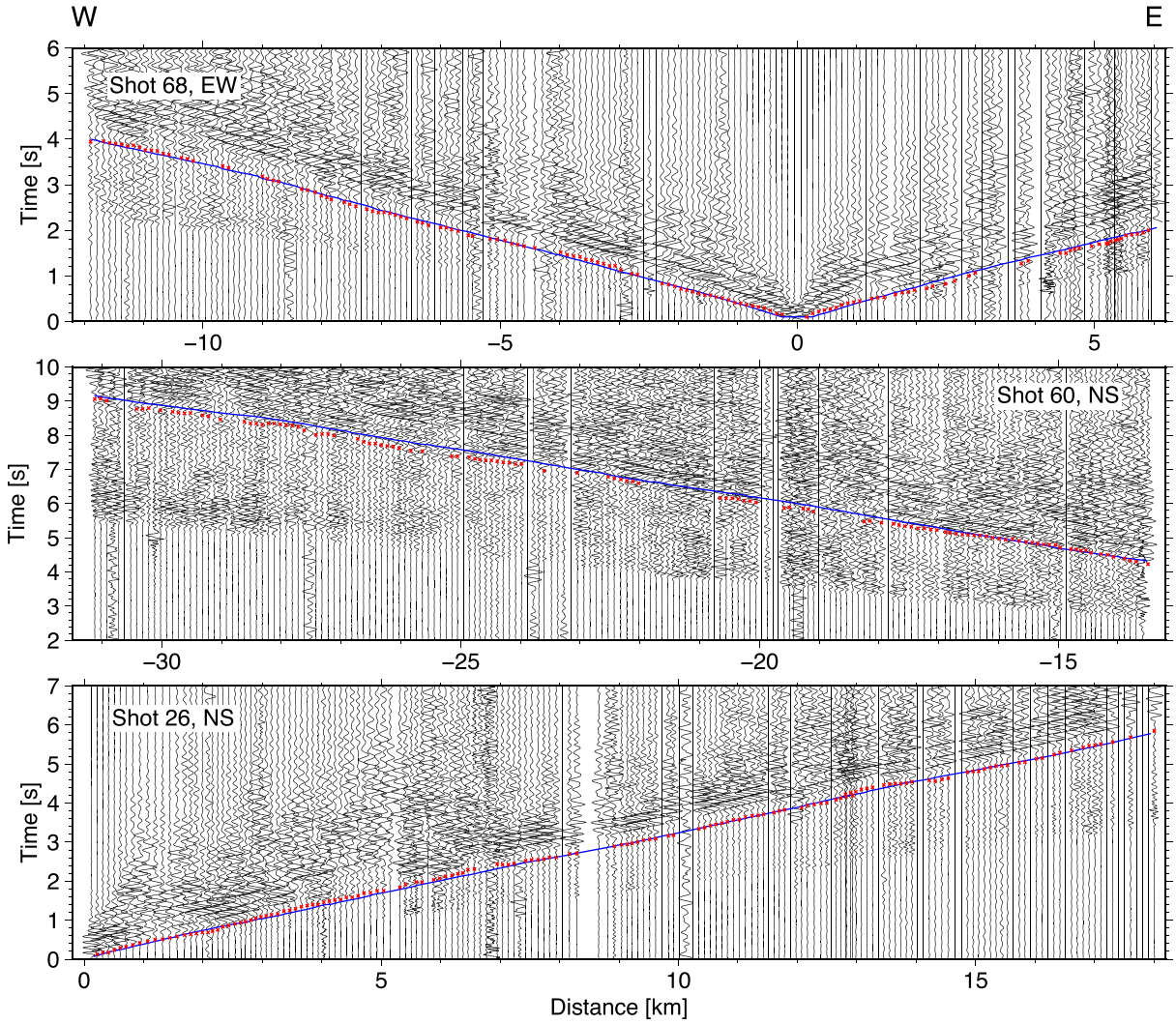

Figure 3. Three shots from the TIPTEQ Seismic experiment recorded by 180 geophones in an 18-km-long geophone spread. Top: Shot 68 (NVR, east–west component). Middle: Shot 60 (ESP, north–south component). Bottom: Shot 26 (NVR, north–south component). Only a bandpass filter (2–9 Hz) was applied to the data, showing the good data quality. *P*-wave arrivals from the three shots are also easily identified. The red dots show the manually picked *S*-wave traveltimes and the blue lines represent theoretical phases calculated from the velocity model obtained with these data. The locations of the shots are shown in Fig. 1.

the techniques described by Lutter *et al.* (1990) and Zelt & Smith (1992). The inverse part of the problem was solved by damped least-squares inversion (e.g. Zelt & Smith 1992; Zelt & Barton 1998) in which an overall damping factor of 10 was employed, allowing a rapid convergence between the theoretical and observed data without introducing significantly large model roughness. The resulting velocity-node updates were added to the already existing velocity values and the forward and inverse problems were carried out again until a suitable convergence between the observed and calculated traveltimes was obtained.

Different *S*-wave velocity models were tested as the initial model for the *S*-wave tomography, including a laterally homogeneous velocity model obtained by fitting a traveltime curve to the observed traveltimes. The final chosen initial model was the *P*-wave velocity model obtained by Micksch (2008), divided by $\sqrt{3}$. The horizontal spacing of the inversion nodes in the velocity model was 2 km and the vertical spacing was 1 km. After eight iterations the rms (root mean square) traveltime residual between observed and theoretical traveltimes was 92 ms and $\chi^2 = 0.71$, with very little improvement in the obtained rms being evident in further iterations. The χ^2 value of 0.71 is close enough to 1 to indicate that the data are adequately but not overfitted, especially if the error estimates for the picked traveltime data have been a little overestimated. All the tested initial models gave similar results in terms of velocity values and velocity anomalies in the upper two kilometres. The criterion for choosing the velocity model resulting from the initial model of Micksch (2008) divided by $\sqrt{3}$, as the final model, was simply that it had the lowest of all rms residual values.

Fig. 4 shows the shear wave tomographic image obtained from the picked traveltimes from TIPTEQ Seismic data. The figure shows a dense ray coverage down to about 2 km below sea level (b.s.l.) between 73.4°W and 72.5°W. As depth increases, the ray coverage becomes less dense, but there are some rays penetrating down to 7 km. However, the resolution test using checkerboard anomalies of 4 km by 2 km shows that such anomalies are only resolvable beneath the central part (Fig. 5), which is spatially coincident with

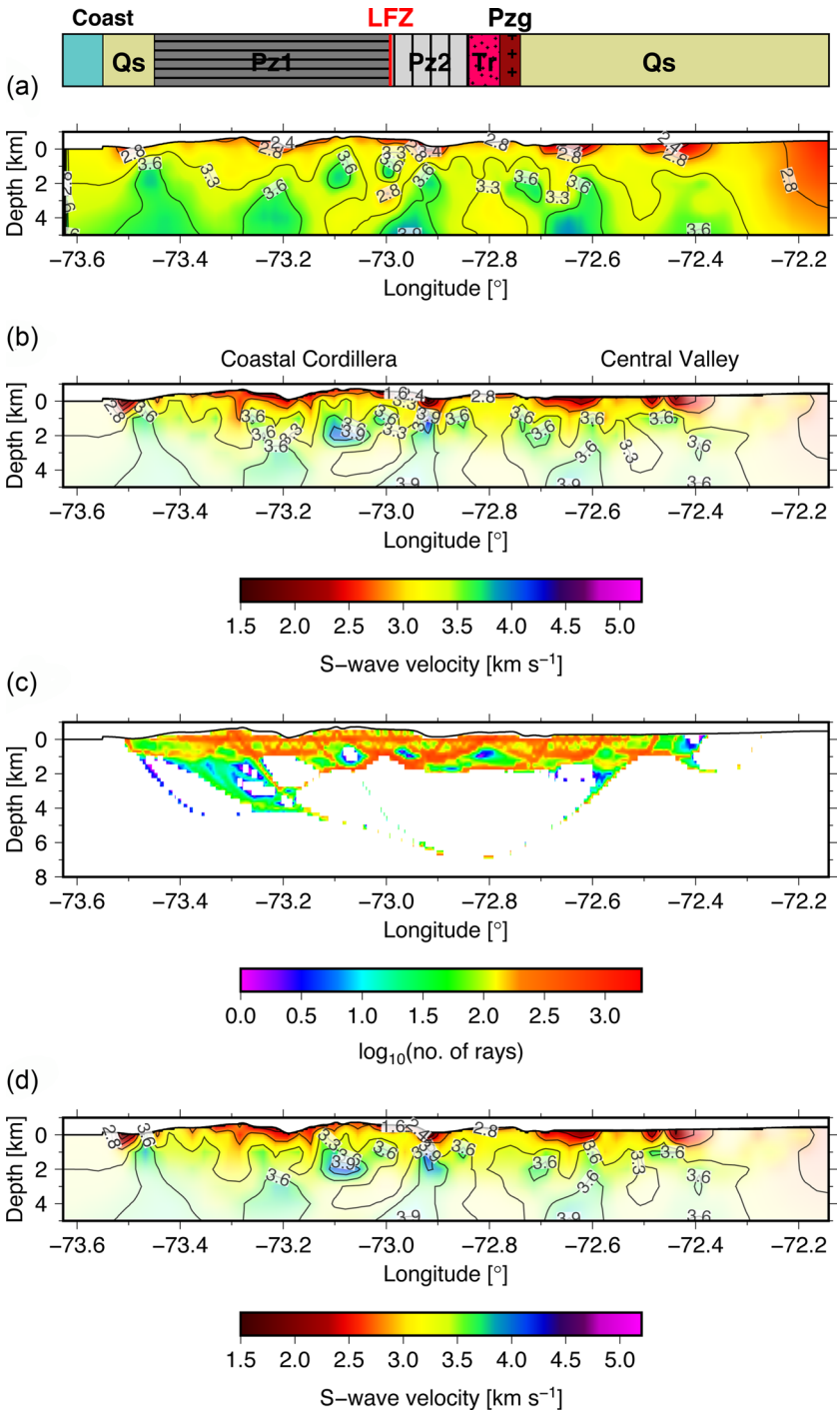

Figure 4. Shear wave tomographic image using *S*-wave arrivals picked on the north–south and east–west components from TIPTEQ Seismic data along the TIPTEQ CDP line. (a) Initial velocity model (Micksch 2008). A geological strip map is also shown (Melnick & Echtler 2006). Qs, undifferentiated sediments (Quaternary); Pz1, western series high-pressure meta-sediments and ultramafics (Permian-Triassic); Pz2, eastern series high-temperature meta-sediments (Carboniferous-Triassic); Tr, rift basin marine, continental and volcanic sequences (Triassic); Pzg, coastal batholith and undifferentiated intrusions (Paleozoic-early Triassic); LFZ, Lanalhue Fault zone. (b) Final velocity model. Brighter regions have good ray coverage and are well resolved whereas fainter regions have poor ray coverage and are poorly resolved. (c) Ray diagram. (d) Model recovery test for which the input traveltime data for the inversion were derived by ray tracing through the model shown in (b).

the densest ray coverage region down to almost 2 km depth (almost 3 km between 73.3°W and 73.1°W). Anomalies of 2 by 1 km are resolvable also beneath the central part of the profile (as seen in the lower resolution test, Fig. 5d), down to 1 km depth and down to 2 km in some regions.

Velocity uncertainties for the velocity model can be observed in Fig. 5(e). During the inversion steps we performed a full matrix inversion to determine a full resolution matrix, which enables the assessment of the model uncertainty (eqs 7–9 in Zelt & Smith 1992). We used an *a priori* estimate of the uncertainties in the velocities of

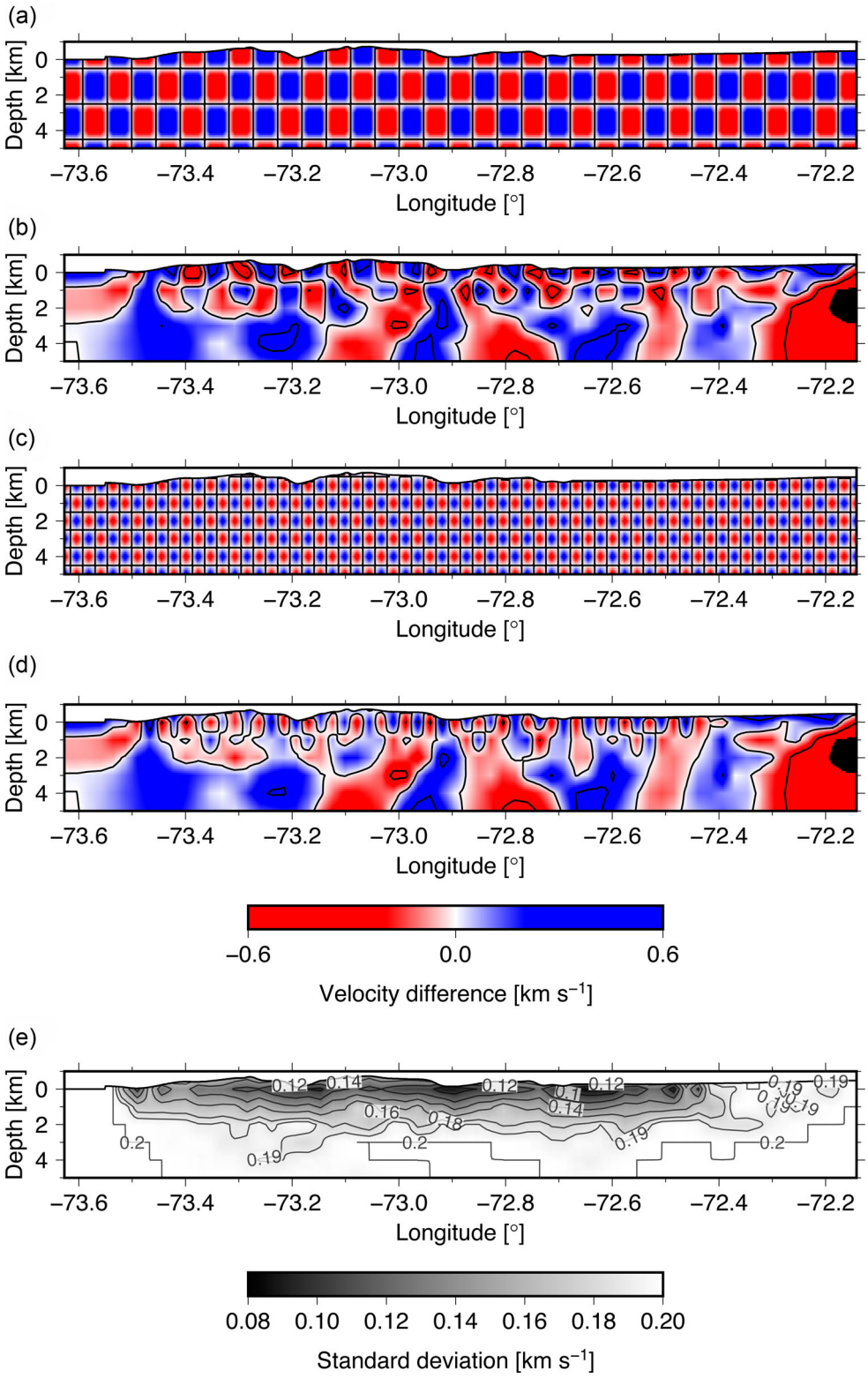

Figure 5. (a) Original checkerboard anomalies of 4 km by 2 km. (b) Retrieved checkerboard anomalies for (a). (c) Original checkerboard anomalies of 2 km by 1 km. (d) Retrieved checkerboard anomalies for panel (c). Amplitude of input anomalies: ±0.3 km s^{-1} relative to reference velocity model. Contours drawn for 0 and ±0.3 km s^{-1}. (e) *S*-wave velocity uncertainties of the final model shown in Fig. 4(b).

0.2 km s^{-1}. By taking the square root of the diagonal elements of the *a posteriori* covariance matrix, the calculated standard errors or uncertainties of the model parameters are obtained (Zelt & Smith 1992). Uncertainties range between 0.08 and 0.2 km s^{-1}, with the lowest values in the topmost part of the velocity model and coinciding with the well resolved area from the checkerboard tests (Figs 5b and d). The factor that primarily contributes to larger uncertainties is the small spacing of the inversion nodes in the velocity model.

The shear wave tomography (Fig. 4b) shows many small-scale structures. Low *S*-wave velocity structures can be observed along the entire profile, just beneath the Coastal Cordillera and the Central Valley. Most of the velocity anomalies in Fig. 4(b), especially in the upper 2 km can be recognized in the *P*-wave velocity tomography of Micksch (2008). However, the resolution and model recovery tests show that some of them cannot be resolved as, for example, the small high-velocity anomaly just at about 73.0°W, which could be an artefact generated during the inversions. Another feature that can be observed in the *S*-wave tomography (and fainter in the *P*-wave tomography) is the presence of vertical velocity anomalies. One such anomaly occurs at 73.3°W, although it is not completely recovered in the model recovery test (Fig. 4d). To date, however, no reflected waves due to a vertical reflector have been observed in the TIPTEQ Seismic data.

5 NOISE TOMOGRAPHY USING THE DATA FROM THE TIPTEQ ARRAY

5.1 Dispersion analysis

The 100 Hz data from the temporary TIPTEQ Seismology array were analysed for observations of ambient seismic noise on the vertical component following Bensen *et al.* (2007). The data processing (filtering, de-trending, normalization), the day-long cross-correlations and the stacking were carried out using the programming language Python, ObsPy (a Python toolbox for processing seismological data; Beyreuther *et al.* 2010) and tools from MIIC (Monitoring and Imaging Based on Interferometric Concepts; Sens-Schönfelder *et al.* 2014). Prior to the calculation of each cross-correlation, the mean value from each daily record was removed. Additionally, the data were high-pass filtered (cut-off frequency: 0.01 Hz), a linear trend was removed and a 1-bit normalization was then applied. The cross-correlation functions for both positive and negative lags were obtained using the convolution theorem. This means that the discrete Fourier transform of the cross-correlation of the two time series equals the product of the Fourier transform of the first times the complex conjugate of the Fourier transform of the second. Working in the frequency domain resulted in being faster in terms of computational resources. The daily cross-correlations were then stacked.

From the 124 EDL stations (see spatial distribution in Fig. 2), we obtained 7542 daily stacked correlations. Fig. 6 shows some resulting cross-correlation functions for station B502. In the observations the source of ambient noise lies primarily in the Pacific ocean. The length of the correlation function depends on the distance between stations. For a small interstation distance it does not take long to observe the Rayleigh waves in the daily stacked correlation function and thus a small number of lags is enough to observe them. The dashed lines in Fig. 6 show where arrivals with a velocity of 3.5 km s^{-1} would be expected. Such arrivals can be observed even in the raw waveforms in Fig. 6.

After the correlation and stacking of the data, a frequency–time analysis (FTAN) was carried out using Python and ObsPy to obtain arrival times for different periods for the dispersive Rayleigh waves. Each correlation function was filtered with 50 different filters centred between 1 and 50 s following Dziewonski *et al.* (1969), thus obtaining filters with different bandwidths. The envelopes of the filtered correlations were calculated and for each of them, the arrival time of the surface wave at the relevant period was calculated as the point of maximum envelope amplitude. FTAN usually showed

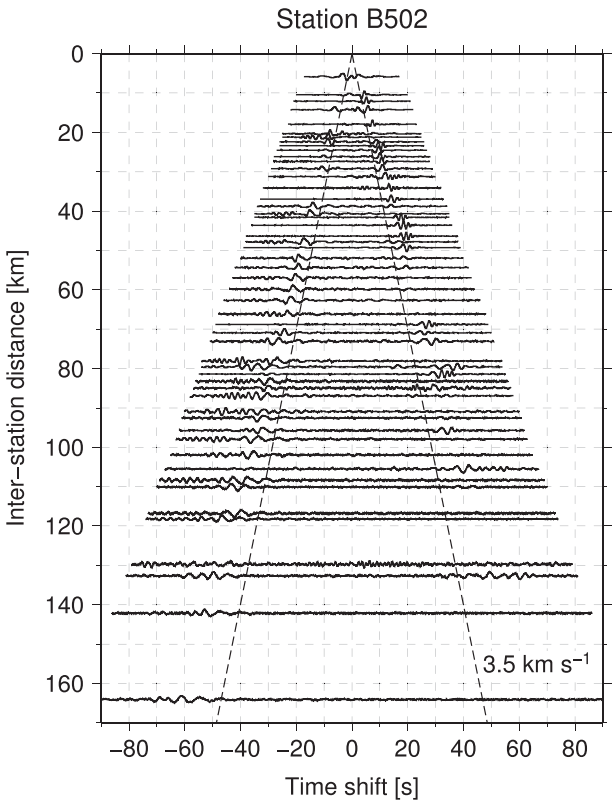

Figure 6. Rayleigh waveforms in the day-long stacked cross-correlations of the data recorded by station B502 (location of this station can be seen in Fig. 2, blue station). The cross-correlations are shown between B502 and 52 other selected stations (for purposes of illustration), plotted according to the interstation distance. The waveforms have not been filtered. The dashed lines show where surface wave arrivals with a velocity of 3.5 km s^{-1} would be expected.

surface wave signals up to a period between 13 and 15 s (depending on the signal-to-noise ratio; see example in Fig. 7), losing seismic energy for longer periods. The sensitivity of surface waves to *S*-wave velocities tells us that good resolution in depth goes down to about one third of the wavelength (e.g. Forsyth *et al.* 1998; Yang & Forsyth 2006). Thus, assuming a surface wave group velocity of ∼3.5 km s^{-1} (see Fig. 6) there should then be a good resolution down to a depth of approximately 17 km in the tomographic inversion. For the 50 picked traveltimes per FTAN, those traveltimes that were shorter than the central period of the applied filter were automatically discarded. When the signal-to-noise ratio was less than 1, the traveltime was also discarded. For the tomographic inversion 19 periods in the range between 2.41 and 15.1 s were used.

5.2 3-D *S*-wave velocity model from inversion of dispersion curves

After FTAN, a direct surface wave inversion for 3-D shear wave velocity structure using the obtained Rayleigh-wave fundamental-mode group velocity curves was carried out after Feng & An (2010) and with the aid of the FTAN software surf96 (Herrmann & Ammon 2002). Unlike traditional inversion schemes in two steps (period-by-period 2-D tomographic inversions for regionalized dispersions and cell-by-cell inversions of regionalized dispersions for 1-D *S*-wave velocity profiles), this scheme combines the two-step inversion equations into one formulation to directly invert dispersion

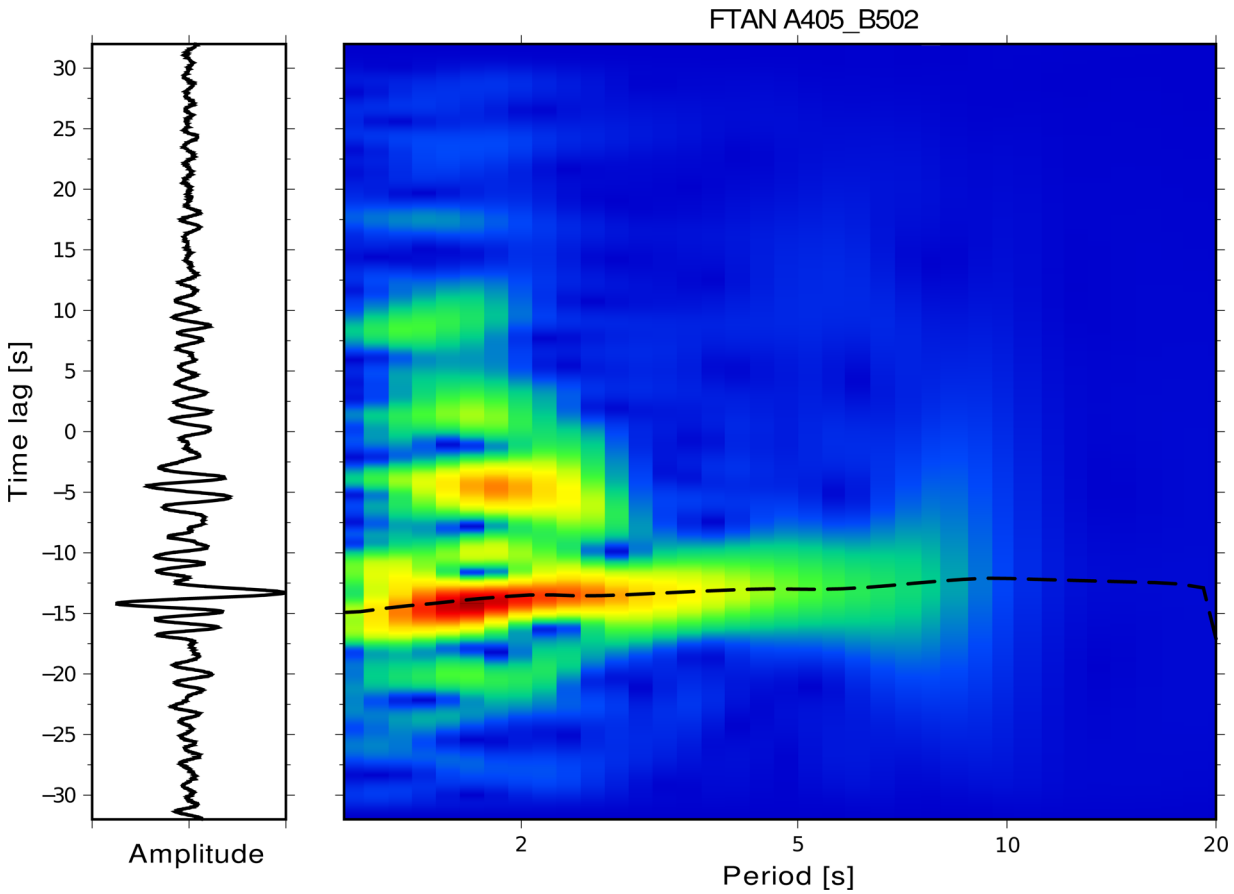

Figure 7. Left: daily stacked cross-correlation for stations B502 and A405. Right: FTAN diagram for stations B502 and A405 (interstation distance: 34.11 km). The locations of the stations can be seen in Fig. 2. The black dashed line represents the measured fundamental-mode group speed curve using the surface wave arrivals for each period (the maximum envelope amplitude). There is signal power until ∼15 s.

curves to 3-D *S*-wave velocities. For the first time this inversion scheme was applied to such a small-scale study. Before the inversion, if the traveltime error divided by the traveltime was larger than 15 per cent, such traveltime data were excluded. Finally, data with an interstation distance shorter than twice the wavelength (λ) of the signal being considered were also removed, leaving a total of 91 276 dispersion measurements for the inversion. The study region was defined between 74°W and 71°W longitude, 37°S and 39.4°S latitude and 0–60 km depth, with a cell size of 0.1° in longitude and latitude and 2 km in depth. The reference model is interpolated from CRUST1.0 (http://igppweb.ucsd.edu/∼gabi/rem.html). Different damping factors were tested, namely, damping factors of 0.5, 1 and 2. Several resolution tests using checkerboards were also carried out. The slice corresponding to the profile along the common depth-point (CDP) line of the TIPTEQ project at latitude 38°15′S, taken from the resulting 3-D *S*-wave velocity model can be seen in Fig. 8. A comparison of the rms misfit of group velocities for the inverted velocity models with each damping factor (Fig. 9) shows no significant differences in the rms for the different damping factors. Thus, finally, a damping factor of 2 was selected, as this produced the smoothest model.

The uncertainties in the observed data (dispersion data) are difficult to determine. However, we can statistically estimate *S*-wave velocity uncertainties using pre-defined observational uncertainties. We assume that group-wave traveltime uncertainties are random and smaller than half a period. Taking the random data uncertainties as synthetic observations, we inverted for a model of 3-D *S*-wave velocity uncertainties using the following linearized equation:

$$\mathbf{G}\Delta = \delta \tag{1}$$

where $\mathbf{G}$ is the sensitivity matrix, $\mathbf{\Delta}$ is the model uncertainty vector and δ is the data uncertainty vector. The velocity model under these assumptions does not include true *S*-wave velocities, but results purely from the supposed data uncertainties and therefore, it can be considered as an *S*-wave velocity uncertainty model. Using 100 groups of random data uncertainties, we obtained 100 velocity uncertainty models. For each spatial position, the average *S*-wave velocity uncertainty over the 100 models is close to 0 km s^{-1}, and the maximum standard deviation throughout the whole 3-D *S*-wave velocity model is 0.033 km s^{-1}, which can be considered as the general uncertainty in the *S*-wave velocities that we inverted for.

The 2-D *S*-wave velocity slice (Fig. 8) shows a relatively smooth transition from velocities of 3.2 km s^{-1} near the surface to 3.6 km s^{-1} at 20 km depth beneath the Coastal Cordillera. At both ends of the profile, beneath the Central Valley and the coastal plain, lower velocities occur near the surface where larger accumulations of sediments and / or volcanics occur.

The tomography using the high-resolution TIPTEQ active source data can resolve well the upper few kilometres beneath the profile, as could be observed in the resolution tests in Figs 4 and 5. It can also resolve much smaller structures and thus, these results are preferred over the results from the noise tomography down to 2 km depth. Moreover, the shortest period used in the surface wave tomographic inversions (2.41 s) gives an indication from where to consider the

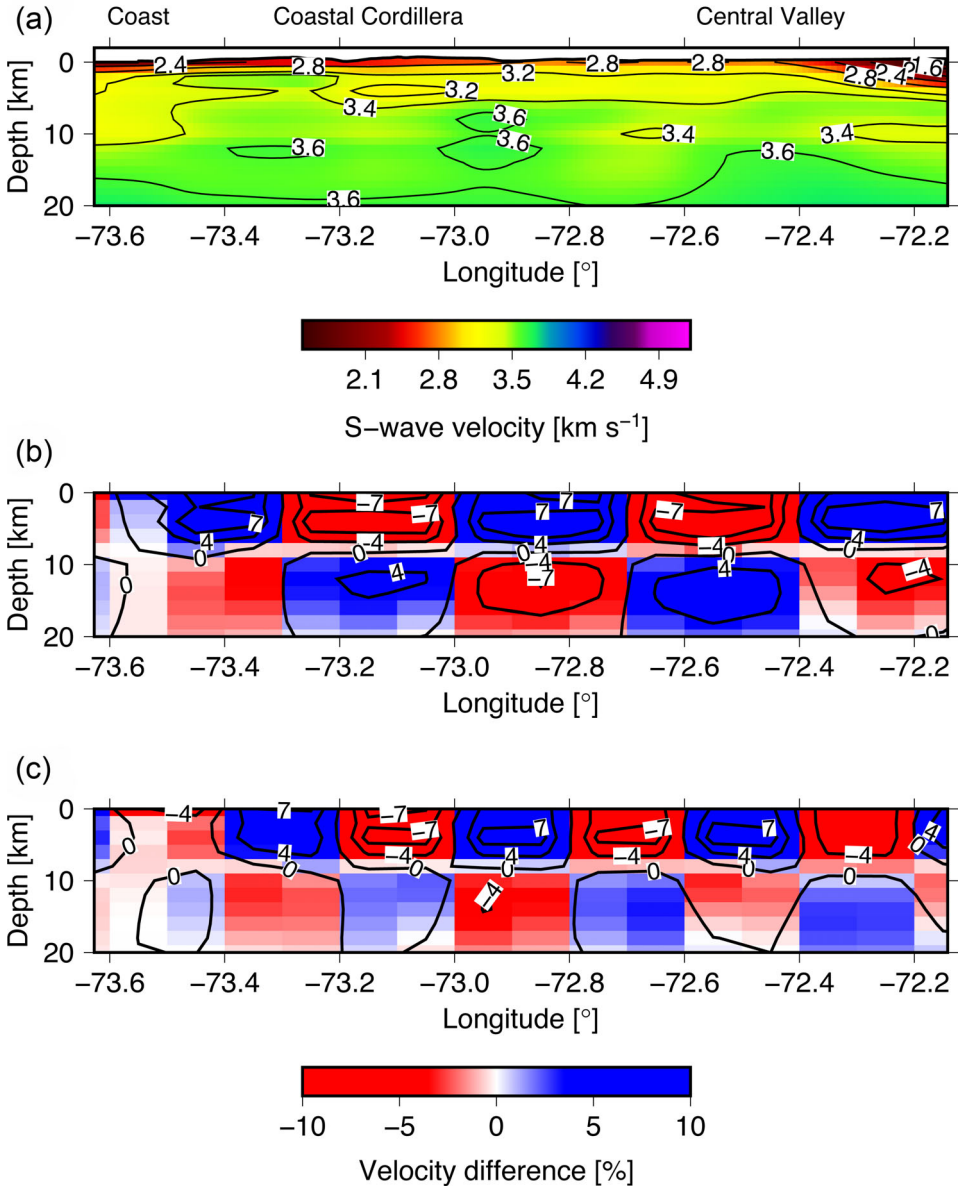

Figure 8. *S*-wave velocity slice corresponding to the latitude 38°15′S taken from the resulting 3-D shear wave velocity model from noise tomography. (a) *S*-wave velocity slice along the TIPTEQ CDP line. Low-velocity anomalies can be observed in the top few kilometres as well as higher velocities in the lower part. (b) Resolution test using checkerboards of dimensions 0.3° times 10 km. (c) Resolution test using checkerboards of 0.2° times 10 km. Amplitude of input anomalies: ±7 per cent relative to the reference velocity model. Contours drawn for 0, ±4 and ±7 per cent.

noise tomography valid (approximately 2 km depth, considering a group velocity of 2.2 km s^{-1}). On the other hand, the longest period used in the inversion, 15.1 s together with the resolution tests using checkerboards (see Fig. 8) allow to take 20 km depth as the lower limit of validity for such anomalies for the velocity model derived from the noise tomography.

5.3 Merging the obtained *S*-wave velocity models with the local earthquake tomographic image

For the lower part of our shear wave velocity model (>20 km depth), the model obtained by Haberland *et al.* (2009) was used. They picked *P*-wave and *S*-wave traveltimes from local earthquake data and *P*-wave traveltimes from the active source data recorded by the TIPTEQ Seismology array to obtain a 2-D *P*-wave tomographic image and a 2-D v_p/v_s ratio model. We took both models and made a grid point division of the *P*-wave velocity values by the v_p/v_s ratio values to obtain an *S*-wave tomogram. Since this model uses local earthquake data it defines very well the area where the Nazca and South American plates interact. Maximum uncertainties are 0.15 km s^{-1} and 0.04 in the *P*-wave velocity model and in the v_p/v_s ratio model respectively (Haberland *et al.* 2009). Thus, the uncertainties in the *S*-wave velocity model from local earthquake tomography can be determined to be smaller than 0.15 km s^{-1} (Topping 1972).

6 RESULTS

Using active and passive source TIPTEQ data recorded along and around a CDP line at 38°15′S, respectively, we obtained shear wave velocity models along the CDP line through traveltime tomography

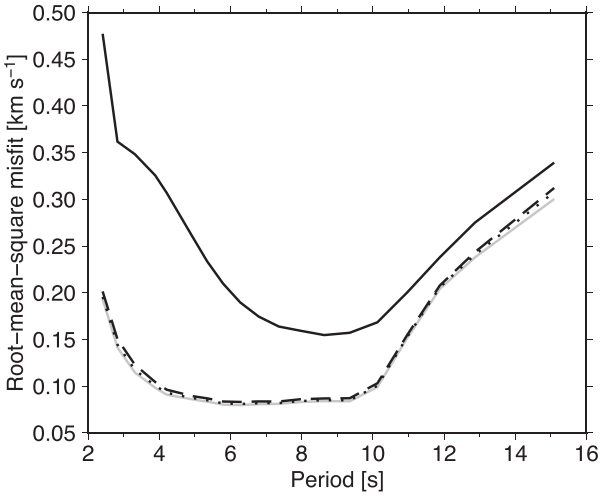

Figure 9. Root mean square (rms) misfit of group velocities for each damping factor. Black solid line: rms fit for the reference velocity model CRUST1.0. Grey line: rms fit for the inverted velocity model with damping factor 0.5. Dotted line: rms fit for the inverted velocity model with damping factor 1. Dashed line: rms fit for the inverted velocity model with damping factor 2.

and noise tomography techniques. It has been shown that each model has a better resolution in a certain depth range. We also had access to an already existent *S*-wave tomogram from local earthquake data, which clearly details the *S*-wave velocities along the plate interface. The obtained *S*-wave velocity model, the already existent *P*-wave velocity models, and the active and passive source TIPTEQ data will allow to carry out further studies about petrophysical properties in the Southern Chile subduction zone. One such study is the derivation of the Poisson's ratio values along the profile.

6.1 Final shear wave velocity model along the transect at 38°15′S

For the final *S*-wave tomographic image, we merged the tomographic models obtained in this study with the local earthquake tomographic image of Haberland *et al.* (2009), such that from 0 to 2 km depth we use the results of the traveltime tomography from the active source data, from 2 to 20 km depth we use the slice at 38°15′S from the 3-D shear wave model from the dispersion analysis and from 20 km to a maximum of 75 km depth, depending on the longitude, we use the *S*-wave velocity model from local earthquake tomography. In general, the models merged well with each other at the boundaries between the individual models at 2 and 20 km depth. However, to get rid of larger velocity contrasts at the boundaries where these do exist (e.g. at the centre of the profile, between the *S*-wave velocity model from noise-tomography and the model from local earthquake tomography, where the latter shows higher velocity values), the velocity values along the profile at 2, 19, 20 and 21 km depth were replaced by the simple average of the velocity at the respective depth and the velocities 1 km above and below (e.g. the new value at 2 km depth was obtained by taking the mean of the values at 1, 2 and 3 km depth). The final *S*-wave velocity model can be observed in Fig. 10. The model has been derived from seismic waves ranging in frequency from 0.06–10 Hz. However, the model from the noise tomography based on the lower frequency waves from 0.06–0.4 Hz does not stick out as either a prominent high or low velocity zone, with respect to either the models from the active source or local earthquake tomography which used waves with higher frequencies from about 1–10 Hz. Indeed, the fact that the different velocity models do seem to blend so well despite the relatively small amount of interpolation between them at around 2 and 20 km depths lends credence to the merging procedure.

6.2 Poisson's ratio model along the transect at 38°15′S

One first study that one can carry out, having a *P*-wave and an *S*-wave velocity model, is to derive a Poisson's ratio model. For an object undergoing stretching, Poisson's ratio is defined as the ratio of the transverse strain to the axial strain. It is commonly used to evaluate the mineralogical composition, porosity, structure and the existence of fluids within a rock.

To obtain the Poisson's ratio model, we needed a *P*-wave velocity model that covered the same area as our *S*-wave velocity model. We used a merged *P*-wave velocity model from TIPTEQ active source data obtained by Micksch (2008) down to 2 km depth and the *P*-wave velocity model from local earthquake tomography obtained by Haberland *et al.* (2009), starting from 2 km and down to 75 km depth. The Poisson's ratio (σ) in terms of the *S*-wave (v_s) and *P*-wave (v_p) velocity is

$$\sigma = \frac{v_p^2 - 2v_s^2}{2\left(v_p^2 - v_s^2\right)} \tag{2}$$

and the Poisson's ratio uncertainty ($\Delta\sigma$) is (see e.g. Contreras-Reyes *et al.* 2008b)

$$\Delta\sigma = \frac{(v_p/v_s)^2}{((v_p/v_s)^2 - 1)^2}\sqrt{\left(\frac{\Delta v_p}{v_p}\right)^2 + \left(\frac{\Delta v_s}{v_s}\right)^2} \tag{3}$$

We applied eq. (2) in a grid point way using our derived *P*-wave and *S*-wave velocity models. The Poisson's ratio model along the transect at 38°15′S can be seen in Fig. 11.

Uncertainties in the topmost part of the Poisson's ratio model (from *P*- and *S*-wave velocity models from the TIPTEQ active source data) can be observed in Fig. 11. The uncertainties in the *P*-wave velocity model from active-source data range between 0.15 and 0.2 km s^{-1}. They are slightly higher than those for the *S*-wave velocity model because of the smaller spacing of 0.5 km horizontally and vertically of the inversion nodes in the *P*-wave velocity model (Micksch 2008). Using eq. (3) we obtain Poisson's ratio uncertainties that range between 0.02 and 0.06 in the area with good ray coverage (Fig. 4c). Down to 2 km depth, uncertainties are 0.05 on average. For depths greater than 2 km, Poisson's ratio uncertainties are calculated from the maximum *P*- and *S*-wave velocity uncertainties. The maximum Poisson's ratio uncertainty is 0.02.

A mean Poisson's ratio value of 0.27 is mostly observed along the profile. This value is essentially the same as the global average of 0.265–0.27 for continental crust (Zandt & Ammon 1995; Christensen 1996). High Poisson's ratio anomalies can also be observed. A clear example is in the central part of the image, between 10 and 20 km depth. This anomaly is significant as it has Poisson's ratios of 0.3–0.31 and the maximum uncertainty in Poisson's ratio is 0.02 in this region. They are also observed as clusters just beneath the surface along the profile and also between the top of the subducting plate and the oceanic Moho. Low Poisson's ratio anomalies are also observed in the first few kilometres depth and under the oceanic Moho. The anomalies in the oceanic crust and mantle are probably significant as they often have Poisson's ratios greater than 0.29 or less than 0.25 and the maximum uncertainty in Poisson's ratio is 0.02 in this region. Together with *P*-wave reflectivity images and seismicity, we interpret the geometry of the LFZ (red line in Fig. 11)

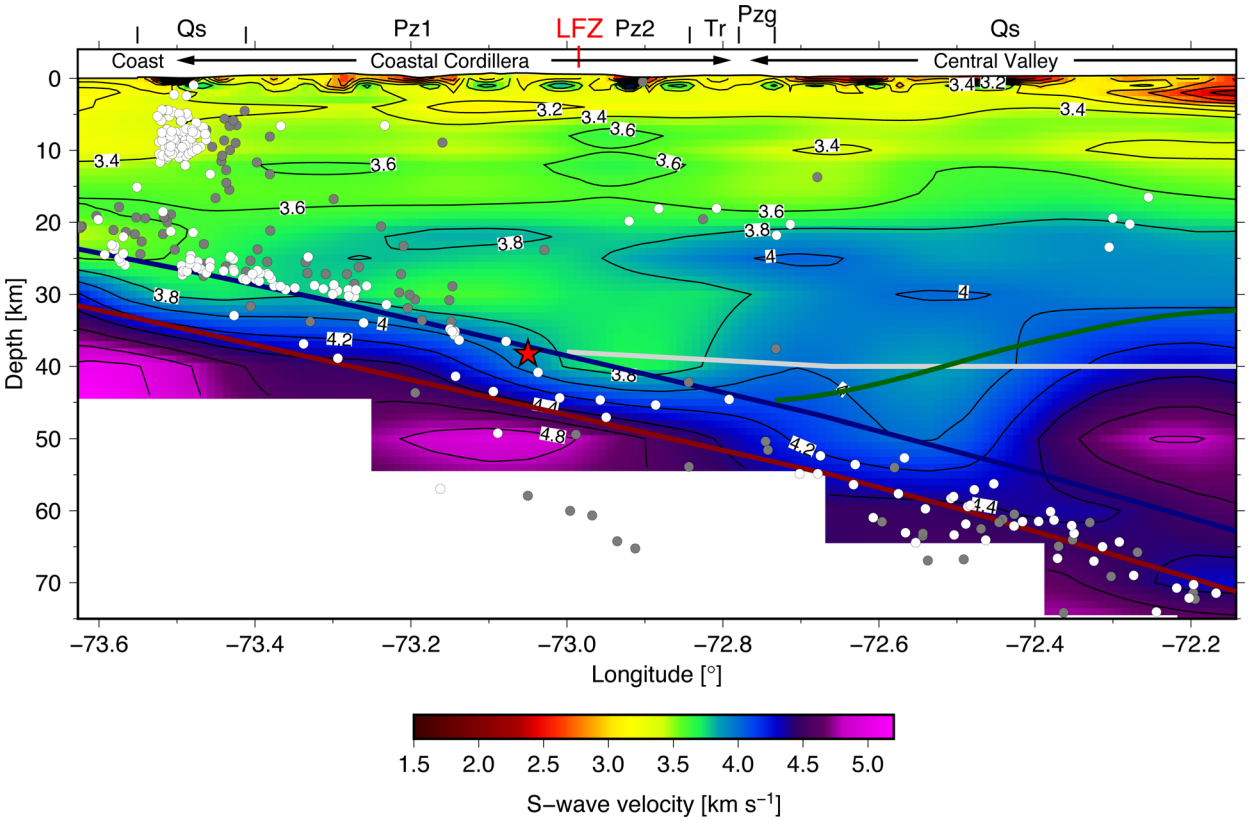

Figure 10. Final *S*-wave velocity tomographic image in Southern Chile along a transect at 38°15′S, obtained by merging three different *S*-wave velocity models, namely a traveltime *S*-wave velocity tomogram using TIPTEQ active source data, an *S*-wave velocity model from noise tomography using data from the TIPTEQ array and an *S*-wave velocity model from local earthquake tomography. The location of the LFZ and the geological units are as in Fig. 4(a). White dots: seismicity along the profile from the TIPTEQ array (Haberland *et al.* 2009). Grey dots: seismicity along the profile from the ISSA 2000 temporary network (Bohm 2004). Red star: hypocentre of the 1960 Valdivia earthquake (Krawczyk & the SPOC Team 2003). Blue line: our interpretation of the geometry of the upper slab boundary. Red and grey lines: oceanic and continental Moho geometry, respectively, from SPOC wide-angle velocity model (Krawczyk & the SPOC Team 2003). Green line: continental Moho geometry from gravity data (Alasonati-Tašárová 2007). See the discussion for further details.

to be east-dipping and such that the fault zone passes close to the eastern edge of the high Poisson's ratio anomaly in the centre of the profile. In particular, a strong, east-dipping reflectivity has been associated to the LFZ (Groß *et al.* 2008; Micksch 2008). This point will be discussed in the next section.

7 DISCUSSION

The use of high resolution active source data allows to obtain a velocity model that can resolve small-scale features, as could be seen in Section 4 and the resolution tests in Fig. 5. The high frequency waves generated by the active sources, although easily recognizable using the appropriate bandpass filter, are quickly attenuated and in consequence their penetration only lasts over a few kilometres depth. We used different sources to cover the lower part of the *S*-wave velocity model. While the *S*-wave velocity model from local earthquake tomography obtained by Haberland *et al.* (2009) describes in good detail the plate interface, noise tomography in the period range between 2.41 and 15.1 s resolves structures in the middle part of the velocity model according to the resolution tests shown in Fig. 8. We see that each of the three velocity models is more adequate for a certain part of the final *S*-wave velocity model. We have been able to merge the different velocity models from different sources to obtain a final *S*-wave velocity model along the transect at 38°15′S. We could interpolate the boundaries between two adjacent models smoothly and mostly without abrupt velocity changes, but it is worth mentioning the ∼0.4 km s^{-1} velocity difference in the centre of the profile at 20 km depth, between the velocity model from noise tomography and the model from local earthquake tomography.

7.1 Comparison between the *S*-wave velocity model from local earthquake tomography and the final merged *S*-wave velocity model

We can compare our final *S*-wave velocity model with the *S*-wave velocity model from local earthquake tomography down to 20 km depth. Fig. 12 shows the *S*-wave velocity values from the model from local earthquake tomography minus the values from our final *S*-wave velocity model. Since from 20 km depth we use the local earthquake tomography in our final model, we show the differences only down to 25 km depth. Velocity differences between 20 and 25 km depth are the product of the interpolation at 20 km depth in our final velocity model. Most of the region between 3 and 20 km depth shows positive differences that do not vary greatly in the model (usually less than 0.3 km s^{-1}). Considering this, it is interesting to note that Fig. 11 shows a region of high Poisson's ratio values in the centre of the profile between 12 and 18 km depth. This feature will be discussed in further detail below.

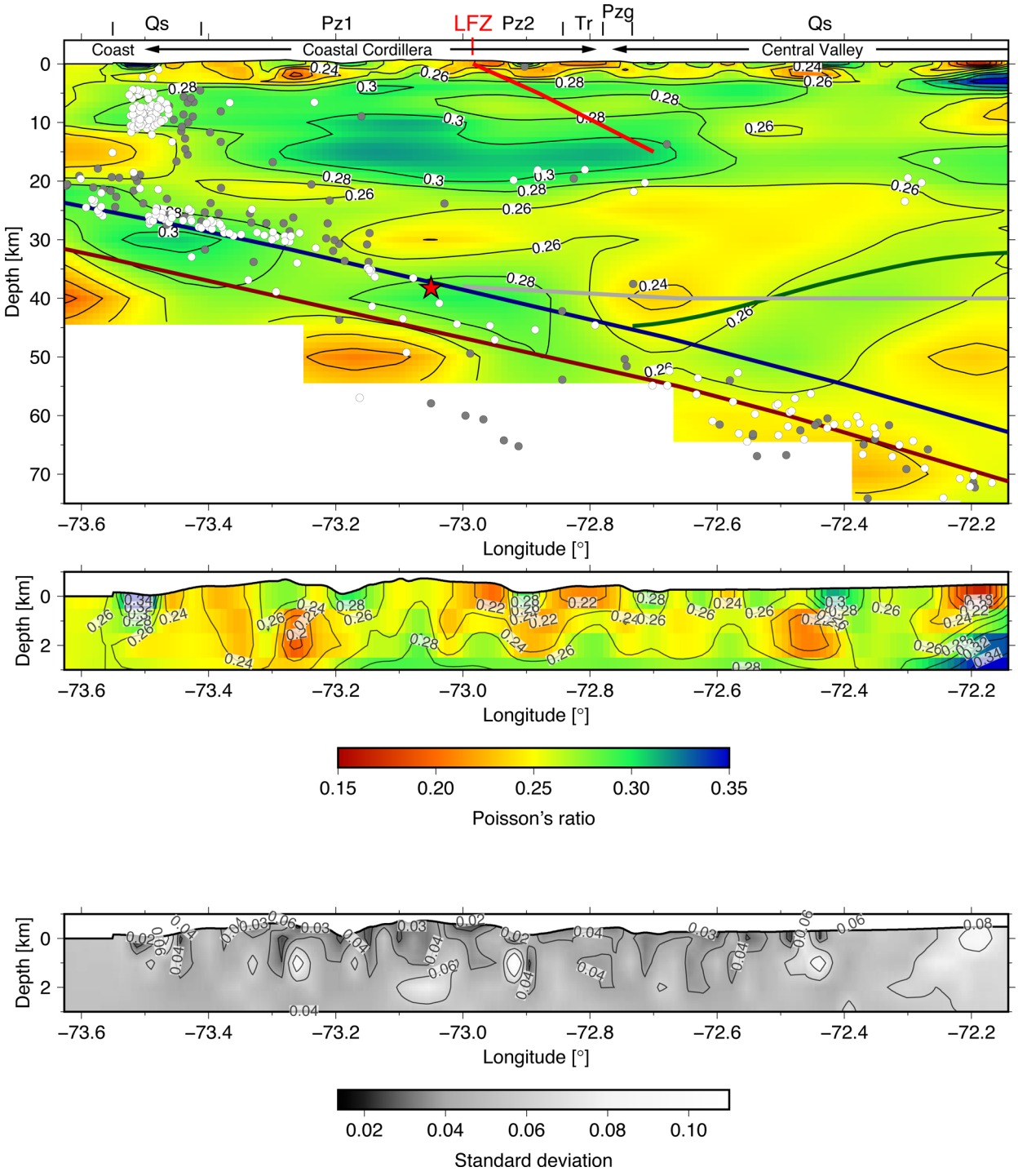

Figure 11. Poisson's ratio image along the transect at 38°15′S. The middle image shows a close-up of the first 3-km depth. The bottom image shows the Poisson's ratio uncertainties in the top kilometres depth of the profile. The geology, the seismicity and the geometry lines are as in Fig. 10. Additionally, the red line is an interpretation of the geometry for the Lanalhue fault zone. See the discussion for further details.

However, the largest velocity differences are observed in the first 2 km depth as small clusters not only with positive differences, but also with some negative differences (see Fig. 12, lower close-up). These clusters show the largest velocity differences in terms of absolute value. This region is where the *S*-wave velocities from local earthquake tomography are compared to the velocities from the controlled source data. Thus, it can be expected to observe such velocity differences because in this region the well resolved, small-scale anomalies from the high-resolution active source data are incorporated in our final *S*-velocity model.

A technical explanation for the velocity differences between the two models between 3 and 20 km depth (where the *S*-wave velocities from noise tomography are used in the final *S*-velocity model), could be the different damping factors used in the inverse part of the tomographic problem for the different models. While certain damping factors might be able to resolve certain velocity anomalies, others

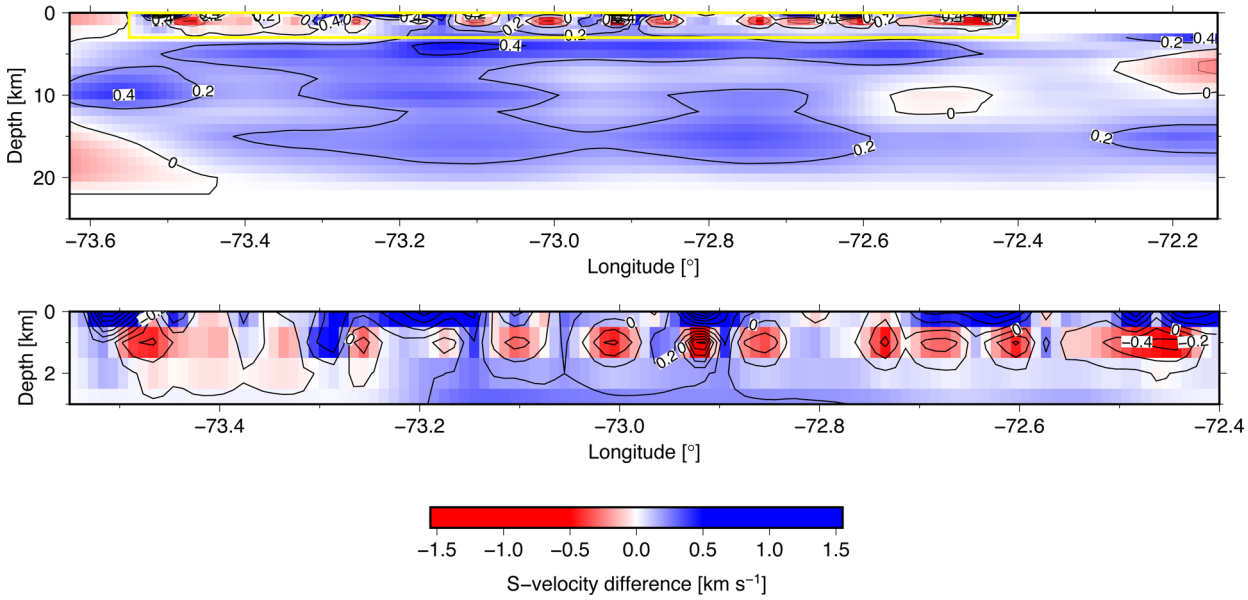

Figure 12. *S*-wave velocity differences (*S*-wave velocities from local earthquake tomography minus final merged *S*-wave velocities in Fig. 10) along the transect at 38°15′S. Most of the region between 3 and 20 km depth has positive velocity differences. There is no information in the local earthquake velocity model down to 1 km depth east of 72.4°W. The lower image shows a close-up of the first 3-km depth.

might not be able to resolve them. Another explanation is related to the different sources used to obtain each velocity model. The noise tomography uses the seismic noise, mainly from the Pacific Ocean, recorded on the vertical component of the stations of the TIPTEQ array. Thus one would expect to obtain v_{SV} velocities from the surface wave (Rayleigh wave) inversion and not v_{SH} velocities. In the case of the local earthquake tomography, *S* waves of both polarities could have been used for the tomographic inversion. This could imply the presence of anisotropy in the continental margin that might explain the *S*-wave velocity differences.

7.2 Velocity anomalies in *S*-wave and *P*-wave velocity models from TIPTEQ controlled source data

The obtained *S*-wave velocity model from TIPTEQ active source data shows velocity anomalies that can be compared to those observed in the *P*-wave velocity model from TIPTEQ active source data obtained by Micksch (2008). These anomalies in both models can be seen in Fig. 4. Similar low-velocity as well as high-velocity anomalies can be observed in both models. High-velocity anomalies between 1 and 2 km depth are repeatedly observed in both models. In the *S*-wave velocity model one such anomaly at 72.9°W reaches particularly high values. Although the resolution tests (Fig. 5) suggest that such a small-scale anomaly is probably difficult to resolve, it is quite faithfully recovered by the model recovery test (Fig. 4d). Similar low-velocity anomalies are observed just beneath the surface in both models, indicating the presence of weathered rock and sedimentary basins. Such anomalies can be observed near the coast at 73.5°W and in the Central Valley at 72.6–72.7°W and 72.35–72.5°W. According to geological maps of the area, young sedimentary rocks are present near the coast and in the central valley (SERNAGEOMIN 2003; Melnick & Echtler 2006). Jordan *et al.* (2001) have shown that late Oligocene-early Miocene sediments in the Central Valley in the study region reach thicknesses of up to 3 km. Some low-velocity sediments are also present within the Coastal Cordillera, where hard metamorphic rocks of Paleozoic age dominate (SERNAGEOMIN 2003). An anomaly with especially low *P*-wave and *S*-wave velocities is located at 72.9°W, east of the LFZ above the high-velocity anomaly mentioned above. The location of this low-velocity anomaly coincides with the location of the eastern series shown in the geological strip map in Fig. 4(a).

7.3 Poisson's ratio model, v_p/v_s ratio model and observed clusters

Eq. (2) shows the relationship between Poisson's ratio (σ, obtained in this study) and the v_p/v_s ratio (Haberland *et al.* 2009). The uppermost part of the downgoing lithosphere, which is characterized by a large-scale v_p/v_s anomaly of about 1.88 (Haberland *et al.* 2009), corresponding to Poisson's ratio values of around 0.28–0.30 (Fig. 11), represents the hydrated oceanic crust that can be observed even down to 70 km depth in the eastern part of the model (Haberland *et al.* 2009; see also the velocities along the subducting lithosphere in Fig. 10). High Poisson's ratios (∼0.28–0.33 in the oceanic crust, ∼0.29 in the upper mantle) are also observed offshore at 43°S (Contreras-Reyes *et al.* 2008b). Strong lithospheric hydration, which was independently corroborated by Tilmann *et al.* (2008) and Contreras-Reyes *et al.* (2008a), occurs due to bending-related faulting at the outer rise offshore. This allows the percolation of sea water down to the upper oceanic mantle (Contreras-Reyes *et al.* 2008a). Poisson's ratios in the oceanic crust and upper mantle are lower onshore than they are offshore, showing the effect of the dehydration of the oceanic plate during the subduction process.

Below the oceanic Moho, which can be observed in Figs 10 and 11 (Krawczyk & the SPOC Team 2003), the Poisson's ratio values locally decrease to values between 0.22–0.26 and thus it is possible to observe the transition between the crust and the upper mantle of the downgoing plate. Unlike in the offshore Poisson's ratio image of Contreras-Reyes *et al.* (2008b), where uniform Poisson's ratios of ∼0.29 are observed in the serpentinized upper mantle, the Poisson's ratios onshore alternate between low values (0.22–0.26) and high values (0.27–0.28). The high Poisson's ratio values would be in agreement with the serpentinization of the subducting oceanic upper mantle.

The observed differences between the Poisson's ratio model obtained in this study (Fig. 11) and the v_p/v_s ratio model of Haberland *et al.* (2009) in the first 2 km depth are due to their different resolution. While the Poisson's ratio model obtained in this study (see Fig. 11) shows a considerable detail of high and low Poisson's ratio clusters, the v_p/v_s model of Haberland *et al.* (2009) shows in general a large low Poisson's ratio body. As discussed above, in relation to the high Poisson's ratio body at 12–18 km depth in the centre of the profile, the possible presence of anisotropy in the continental margin might explain the difference in velocities and Poisson's ratios derived when using data from different sources.

Low-velocity anomalies in the *P*-wave or *S*-wave velocity models just beneath the surface that were related to sediments in the Central Valley and the Coastal Cordillera according to the geological map do not always correlate clearly to specific Poisson's ratio anomalies in Fig. 11. Nevertheless, some of them are correlated to high Poisson's ratio anomalies (e.g. at 73.5°W, 72.9°W, east of 73.2°W and 72.4°W).

Another interesting feature is the large region of high Poisson's ratio values between 0.3 and 0.31 at the centre of the model between 12 and 18 km depth (Fig. 11). This region had already been recognized to have high v_p/v_s ratios of 1.77–1.82 (Haberland *et al.* 2009). The high Poisson's ratio values between 0.3 and 0.31 beneath the centre of the model between 12 and 18 km depth are associated with *S*-velocities of about 3.6 km s^{-1} and thus *P*-velocities between 6.7 and 7.0 km s^{-1}. Assuming that the velocities are unaffected by anisotropy (but see discussion above in Section 7.1), then searching in a data bank containing velocity measurements for 416 rocks of different types (Stadtlander *et al.* 1999 and references therein) reveals that granulite, anorthosite, gabbro and partially serpentinized peridotite are possible rock types having the appropriate *P*- and *S*-velocities and thus appropriate Poisson's ratios at 12–18 km depth below the central part of the transect at 38°15′S. Thus, the values in the obtained Poisson's ratio model can be explained by such rock types. Granulite, anorthosite and gabbro are also in the database of Christensen (1996). The Poisson's ratios of these rock types in this database are also in agreement with the values in the obtained Poisson's ratio model at 12–18 km depth below the central part of the transect. Apart from anorthosite, the other three rock types are either found exposed in the western series (partially serpentinized peridotite) or their metamorphic equivalents are found exposed in the western series (gabbro) or they could be deeper crustal equivalents of rocks exposed in the western series (granulite; e.g. Hervé 1988; Glodny *et al.* 2008). If the region with high Poisson's ratio in the centre of the model between 12 and 18 km depth represents the extension at depth of the western series, then the LFZ, which separates the eastern and western series (Glodny *et al.* 2008), must dip towards the E or NE, in agreement with the interpretation of *P*-wave reflectivity images (Micksch 2008) and geological cross-sections (Glodny *et al.* 2008). The presence of present-day fluids is not necessary to explain Poisson's ratio and v_p/v_s ratio values. This could imply a lack of measurable amounts of present-day fluids according to the seismic velocities above the plate interface in the continental crust of the Coastal Cordillera and the Central Valley in this part of the convergent margin. This is, in turn, in agreement with the high-quality reflectivity images along the profile (Groß *et al.* 2008; Micksch 2008). It is also in agreement, as will be discussed in more detail below, with a model for water being transported down and released from the subduction zone (Völker & Stipp 2015).

7.4 Correlating *S*-wave velocity and Poisson's ratio models to other studies

Figs 10 and 11 show the correlation of our final *S*-wave velocity and Poisson's ratio models respectively, to the results of other studies. The hypocentre of the Valdivia earthquake, primarily studied by Cifuentes (1989), was relocated by Krawczyk & the SPOC Team (2003). The local seismicity recorded by the TIPTEQ temporary array (white dots in Figs 10 and 11) comprises the relocated events in the 3-D velocity model of Haberland *et al.* (2009), while that recorded by the ISSA 2000 temporary array (grey dots in Figs 10 and 11) consists of events located in the 1-D velocity model of Bohm (2004). The oceanic (dark red line in Figs 10 and 11) and continental Moho geometries (grey line in Figs 10 and 11) from the SPOC wide-angle data are determined as the depths where *P*-wave velocities of 8 km s^{-1} and 7.2 km s^{-1} respectively are attained (Krawczyk *et al.* 2006 and references therein). The oceanic Moho depths coincide with the top of the region of alternating high and low Poisson's ratio anomalies (Fig. 11). A different interpretation for the continental Moho geometry (green line) from a 3-D density model from gravity data is offered by Alasonati-Tašárová (2007). The dark blue line in Figs 10 and 11 is our interpretation of the geometry of the upper slab boundary using jointly the local seismicity and reflectivity images along the profile (C. Haberland, private communication, 2015; Micksch 2008), resulting in an oceanic crust ∼7 km thick. This is in agreement with Nazca plate oceanic crustal thicknesses from other studies (e.g. Krawczyk *et al.* 2006; Contreras-Reyes *et al.* 2008a).

Due to bending-related faulting at the outer rise offshore, the oceanic crust and upper mantle are hydrated (Contreras-Reyes *et al.* 2008a), explaining high Poisson's ratios observed offshore (∼0.28–0.33 in the oceanic crust and ∼0.29 in the upper mantle) (Contreras-Reyes *et al.* 2008b). Onshore, however, these values decrease. In particular, we observe in the subducting oceanic crust Poisson's ratios of 0.27–0.31 in the western part of the profile, until 72.8°W and 0.25–0.27 east of 72.8°W. A study from Völker & Stipp (2015) could explain this observation. They ran thermal models to estimate the amount of water carried into the south-central Chile subduction zone and released by the oceanic crust and mantle for Nazca plate segments of different age. Considering a segment with an age of 25 million years appropriate for our study region (Sdrolias & Müller 2006), the oceanic crust would lose ∼10 per cent of the initial water content when it reaches the coast. Then the water content remains constant until ∼70 km from the coast. East of this point, it begins to release water again. At 38.25°S, at 70 km from the coast (or at ∼72.83°W), the continental Moho is already above the subducting oceanic plate (see Fig. 11). This supports the idea, already mentioned above, of a continental crust above the subducting plate showing no indications of present-day measurable amounts of fluids in terms of seismic velocities. On the other hand, it supports the existence of a serpentinized continental mantle wedge, already proposed from seismological, gravity and resistivity studies (Krawczyk *et al.* 2006; Haberland *et al.* 2009; Kapinos 2011). According to Völker & Stipp (2015), the release of water to the overlying continental mantle would not be much. However, if it has been happening over a long period of time it could add up to a significant process.

Again using the *P*-wave reflectivity images (e.g. from Micksch 2008) and also events that were localized along the LFZ (Haberland *et al.* 2006), we interpret a geometry for the LFZ, seen as the red line in Fig. 11. The seismic activity associated with the LFZ and other strike-slip faults in the area, and which is located between

10 and 30 km depth, suggests deep reaching near-vertical faults (Haberland *et al.* 2006). However, as already mentioned above, an east-dipping fault plane instead of a purely vertical strike-slip fault seems better supported by the *P*-wave reflectivity images and the geological cross-sections (Glodny *et al.* 2008; Micksch 2008). The proposed geometry for the LFZ, coincides with the location of the eastern end of the high Poisson's ratio anomaly that we interpreted as the extension at depth of the western series.

ACKNOWLEDGEMENTS

The project TIPTEQ was funded by the German Ministry of Education and Research (BMBF), the German Research Foundation (DFG) and benefited from grants of the Free University of Berlin and the GFZ Potsdam. The instruments for the TIPTEQ experiments were provided by the Geophysical Instrument Pool Potsdam (GIPP) and the Free University of Berlin. C. Haberland kindly provided the *P*-wave velocity and the v_p/v_s ratio models from the local earthquake tomography and also contributed to the discussion of the geometry of the upper slab boundary. We thank the editor Jun Korenaga and two reviewers whose comments and suggestions helped improve this paper. The figures were made with the GMT program (Wessel *et al.* 2013). CR is supported by the German Academic Exchange Service (DAAD).

REFERENCES

Alasonati-Tašárová, Z., 2007. Towards understanding the lithospheric structure of the southern Chilean subduction zone (36°S–42°S) and its role in the gravity field, *Geophys. J. Int.,* **170**(3), 995–1014.

Bensen, G.D., Ritzwoller, M.H., Barmin, M.P., Levshin, A.L., Lin, F., Moschetti, M.P., Shapiro, N.M. & Yang, Y., 2007. Processing seismic ambient noise data to obtain reliable broad-band surface wave dispersion measurements, *Geophys. J. Int.,* **169**(3), 1239–1260.

Beyreuther, M., Barsch, R., Krischer, L., Megies, T., Behr, Y. & Wassermann, J., 2010. ObsPy: a Python toolbox for seismology, *Seismol. Res. Lett.,* **81**(3), 530–533.

Bohm, M., 2004. 3D Lokalbebentomographie der südlichen Anden zwischen 36° und 40°S. *PhD thesis,* freie Universität Berlin and Deutsches GeoForschungsZentrum Potsdam. Scientific Technical Report STR04/15, Available at: http://www.gfz-potsdam.de/bib/pub/str0415/0415.pdf.

Christensen, N.I., 1996. Poisson's ratio and crustal seismology, *J. geophys. Res.,* **101**(B2), 3139–3156.

Cifuentes, I.L., 1989. The 1960 Chilean earthquakes, *J. geophys. Res.,* **94**(B1), 665–680.

Contreras-Reyes, E., Grevemeyer, I., Flüh, E.R. & Reichert, C., 2008a. Upper lithospheric structure of the subduction zone offshore of southern Arauco peninsula, Chile, at ∼38°S, *J. geophys. Res.,* **113**(B7), B07303, doi:10.1029/2007JB005569.

Contreras-Reyes, E., Grevemeyer, I., Flüh, E.R., Scherwath, M. & Bialas, J., 2008b. Effect of trench-outer rise bending-related faulting on seismic Poisson's ratio and mantle anisotropy: a case study offshore of Southern Central Chile, *Geophys. J. Int.,* **173**(1), 142–156.

Dohr, G., 1985. Development of a procedure for the exploration of areas with poor reflections by the combined application of different geophysical methods, taking the North-West German basin as an example, in *New Technologies for the Exploration and Exploitation of Oil and Gas Resources,* pp. 62–69, eds De Bouw, R., Millich, E., Joulia, J. & Van Asselt, D., Graham and Trotman.

Dziewonski, A., Bloch, S. & Landisman, M., 1969. A technique for the analysis of transient seismic signals, *Bull. seism. Soc. Am.,* **59**(1), 427–444.

Feng, M. & An, M., 2010. Lithospheric structure of the Chinese mainland determined from joint inversion of regional and teleseismic Rayleigh-wave group velocities, *J. geophys. Res.,* **115**(B6), B06317, doi:10.1029/2008JB005787.

Forsyth, D.W., Webb, S.C., Dorman, L.M. & Shen, Y., 1998. Phase velocities of Rayleigh waves in the MELT experiment on the East Pacific Rise, *Science,* **280**(5367), 1235–1238.

Glodny, J., Echtler, H., Collao, S., Ardiles, M., Burón, P. & Figueroa, O., 2008. Differential Late Paleozoic active margin evolution in South-Central Chile (37°S–40°S)—the Lanalhue Fault Zone, *J. South Am. Earth Sci.,* **26**(4), 397–411.

Groß, K., Micksch, U. & TIPTEQ research group, 2008. The reflection seismic survey of project TIPTEQ - the inventory of the Chilean subduction zone at 38°S, *Geophys. J. Int.,* **172**(2), 565–571.

Haberland, C., Rietbrock, A., Lange, D., Bataille, K. & Hoffmann, S., 2006. Interaction between forearc and oceanic plate at the southcentral Chilean margin as seen in local seismic data, *Geophys. Res. Lett.,* **33**(23), L23302, doi:10.1029/2006GL028189.

Haberland, C., Rietbrock, A., Lange, D., Bataille, K. & Damm, T., 2009. Structure of the seismogenic zone of the south-central Chilean margin revealed by local earthquake travel-time tomography, *J. geophys. Res.,* **114**(B1), B01317, doi:10.1029/2008JB005802.

Herrmann, R.B. & Ammon, C.J., 2002. *Computer Programs in Seismology—Surface Waves, Receiver Functions and Crustal Structure,* St. Louis University, Available at: http://www.eas.slu.edu/eqc/eqc_cps/CPS/CPS330.html.

Hervé, F., 1988. Late Paleozoic subduction and accretion in Southern Chile, *Episodes,* **11**(3), 183–188.

Jordan, T.E., Burns, W.M., Veiga, R., Pángaro, F., Copeland, P., Kelley, S. & Mpodozis, C., 2001. Extension and basin formation in the southern Andes caused by increased convergence rate: A mid-Cenozoic trigger for the Andes, *Tectonics,* **20**(3), 308–324.

Kapinos, G., 2011. Amphibious magnetotellurics at the south-central Chilean continental margin, *PhD thesis,* freie Universität Berlin, Available at: http://www.diss.fu-berlin.de/diss/receive/FUDISS_thesis_000000024773.

Kendrick, E., Bevis, M., Smalley, R., Brooks, B., Vargas, R.B., Lauria, E. & Fortes, L.P.S., 2003. The Nazca-South America Euler vector and its rate of change, *J. South Am. Earth Sci.,* **16**(2), 125–131.

Krawczyk, C. & the SPOC Team, 2003. Amphibious seismic survey images plate interface at 1960 Chile earthquake, *EOS, Trans. Am. geophys. Un.,* **84**(32), 301–305.

Krawczyk, C. *et al.*, 2006. Geophysical signatures and active tectonics at the south-central Chilean margin , in *The Andes – Active Subduction Orogeny. Frontiers in Earth Science,* Vol. 1, pp. 171–192, eds Oncken, O., Chong, G., Franz, G., Giese, P., Götze, H., Ramos, V., Strecker, M. & Wigger, P., Springer Verlag.

Lutter, W.J., Nowack, R.L. & Braile, L.W., 1990. Seismic imaging of upper crustal structure using travel times from the PASSCAL Ouachita experiment, *J. geophys. Res.,* **95**(B4), 4621–4631.

Melnick, D. & Echtler, H., 2006. Morphotectonic and geologic digital map compilations of the south-central Andes (36–43°S), in *The Andes – Active Subduction Orogeny. Frontiers in Earth Science,* Vol. 1, pp. 565–568, eds Oncken, O., Chong, G., Franz, G., Giese, P., Götze, H., Ramos, V., Strecker, M. & Wigger, P., Springer Verlag.

Micksch, U., 2008. The Chilean subduction zone at 38°S: new geophysical images derived from seismic reflection data of project TIPTEQ; implications for the subduction channel and the seismogenic coupling zone, *PhD thesis,* freie Universität Berlin and Deutsches GeoForschungsZentrum Potsdam. Scientific technical report STR 08/14.

Podvin, P. & Lecomte, I., 1991. Finite difference computation of travel times in very contrasted velocity models: a massive parallel approach and its associated tools, *Geophys. J. Int.,* **105**(1), 271–284.

Rietbrock, A., Haberland, C., Bataille, K., Dahm, T. & Oncken, O., 2005. Studying the seismogenic coupling zone with a passive seismic array, *EOS, Trans. Am. geophys. Un.,* **86**(32), 293–297.

Scherwath, M., Flüh, E., Grevemeyer, I., Tilmann, F., Contreras-Reyes, E. & Weinrebe, W., 2006. Investigating subduction zone processes in Chile, *EOS, Trans. Am. geophys. Un.,* **87**(27), 265–272.

Scherwath, M., Contreras-Reyes, E., Flüh, E.R., Grevemeyer, I., Krabbenhöft, A., Papenberg, C., Petersen, C.J. & Weinrebe, R.W., 2009.

Deep lithospheric structures along the southern central Chile margin from wide-angle P-wave modelling, *Geophys. J. Int.,* **179**(1), 579–600.

Schneider Jr., W.A., Ranzinger, K. A., Balch, A.H. & Kruse, C., 1992. A dynamic programming approach to first arrival travel-time computation in media with arbitrarily distributed velocities, *Geophysics,* **57**(1), 39–50.

Sdrolias, M. & Müller, R.D., 2006. Controls on back-arc basin formation, *Geochem. Geophys. Geosyst.,* **7**(4), Q04016, doi:10.1029/2005GC001090.

Sens-Schönfelder, C. *et al.*, 2014. MIIC: Monitoring and Imaging Based on Interferometric Concepts, in *Tomography of the Earth's Crust: From Geophysical Sounding to Real-Time Monitoring,* pp. 43–61, eds Weber, M. & Münch, U., Springer International Publishing.

SERNAGEOMIN, 2003. Mapa geológico de Chile, versión digital, No. 4 (CD-ROM, versión 1.0, 2003), Servicio Nacional de Geología y Minería, Santiago de Chile.

Stadtlander, R., Mechie, J. & Schulze, A., 1999. Deep structure of the southern Ural mountains as derived from wide-angle seismic data, *Geophys. J. Int.,* **137**(2), 501–515.

Tilmann, F.J., Grevemeyer, I., Flüh, E.R., Dahm, T. & Gossler, J., 2008. Seismicity in the outer rise offshore southern Chile: indication of fluid effects in crust and mantle, *Earth planet. Sci. Lett.,* **269**(1–2), 41–55.

Topping, J., 1972. *Errors of Observation and their Treatment,* Chapman and Hall, 119 pp.

Vidale, J., 1988. Finite-difference calculation of travel times, *Bull. seism. Soc. Am.,* **78**(6), 2062–2076.

Völker, D. & Stipp, M., 2015. Water input and water release from the subducting Nazca Plate along southern Central Chile (33°S–46°S), *Geochem. Geophys. Geosyst.,* **16**(6), 1825–1847.

Wessel, P., Smith, W.H. F., Scharroo, R., Luis, J. & Wobbe, F., 2013. Generic Mapping Tools: Improved Version Released, *EOS, Trans. Am. geophys. Un.,* **94**(45), 409–410.

Yang, Y. & Forsyth, D.W., 2006. Regional tomographic inversion of the amplitude and phase of Rayleigh waves with 2-D sensitivity kernels, *Geophys. J. Int.,* **166**(3), 1148–1160.

Zandt, G. & Ammon, C.J., 1995. Continental crust composition constrained by measurements of crustal Poisson's ratio, *Nature,* **374**(6518), 152–154.

Zelt, C.A. & Barton, P.J., 1998. Three-dimensional seismic refraction tomography: a comparison of two methods applied to data from the Faeroe Basin, *J. geophys. Res.,* **103**(B4), 7187–7210.

Zelt, C.A. & Smith, R.B., 1992. Seismic travel-time inversion for 2-D crustal velocity structure, *Geophys. J. Int.,* **108**(1), 16–34.